



Kumar, D., Hargreaves, J., Bharj, A., Scorrer, A., Harding, L. M., Dominguez Andrade, H., Holmes, R., Burrows, R. W., Dawson, H., Warren, A. D., Flewitt, P. E. J., & Martin, T. L. (2021). The Effects of Fusion Reactor Thermal Transients on the Microstructure of Eurofer-97 Steel. *Journal of Nuclear Materials*, 554, [153084].
<https://doi.org/10.1016/j.jnucmat.2021.153084>

Publisher's PDF, also known as Version of record

License (if available):
CC BY

Link to published version (if available):
[10.1016/j.jnucmat.2021.153084](https://doi.org/10.1016/j.jnucmat.2021.153084)

[Link to publication record in Explore Bristol Research](#)
PDF-document

This is the final published version of the article (version of record). It first appeared online via Elsevier at <https://doi.org/10.1016/j.jnucmat.2021.153084> . Please refer to any applicable terms of use of the publisher.

University of Bristol - Explore Bristol Research

General rights

This document is made available in accordance with publisher policies. Please cite only the published version using the reference above. Full terms of use are available:
<http://www.bristol.ac.uk/red/research-policy/pure/user-guides/ebr-terms/>



The effects of fusion reactor thermal transients on the microstructure of Eurofer-97 steel



D. Kumar^{a,*}, J. Hargreaves^a, A. Bharj^a, A. Scorrer^a, L.M. Harding^a, H. Dominguez-Andrade^a, R. Holmes^b, R. Burrows^b, H. Dawson^c, A.D. Warren^a, P.E.J. Flewitt^a, T.L. Martin^a

^a University of Bristol, H.H. Wills Physics Laboratory, Tyndall Avenue, Bristol BS8 1TL, UK

^b National Nuclear Laboratory, Chadwick House, Birchwood Park, Warrington, Cheshire, WA3 6AE, UK

^c UKAEA, Culham Centre for Fusion Energy, Culham Science Centre, Abingdon, Oxfordshire, OX14 3DB, England

ARTICLE INFO

Article history:

Received 16 November 2020

Revised 26 January 2021

Accepted 13 May 2021

Available online 19 May 2021

Keywords:

Fusion
Martensite
Microstructure
Thermal effects
Modelling

ABSTRACT

Plasma-wall interactions in a commercial-scale fusion power station may exert high transient thermal loads on plasma-facing surfaces, repeatedly subjecting underlying structural materials to high temperatures for short durations. Specimens of the reduced activation ferritic-martensitic steel Eurofer-97 were continuously aged at constant temperature in the range of 550°C to 950°C for up to 168 hours in a furnace to investigate the microstructural effects of short-term high temperature exposure. A CO₂ laser was also used to repeatedly heat another specimen from 400°C to 850°C a total of 1,480 times over a period of 41 hours to explore transient heating effects. Microstructural changes were studied via scanning electron and focused ion beam microscopy and include (i) the coarsening of Cr-rich secondary phase precipitates when continuously heated above 750°C, (ii) an increase in average grain size above 800°C and (iii) the evolution of a new lath martensite microstructure above 850°C. Conversely, transient heating via a laser was found to result in the decomposition of the as-received lath martensite structure into ferrite and Cr-rich carbide precipitates, accompanied by a significant increase in average grain size from 0.1–2 μm to 5–40 μm. Experimental analysis was supported by thermodynamic simulation of the equilibrium phase behaviour of Eurofer-97 in MatCalc and thermal finite element modelling of plasma-wall interaction heating on the water-cooled lithium-lead tritium breeding blanket concept in Comsol Multiphysics. Simulated thermal transients were found to significantly alter the microstructure of Eurofer-97 and the implications of this are discussed.

© 2021 The Author(s). Published by Elsevier B.V.

This is an open access article under the CC BY license (<http://creativecommons.org/licenses/by/4.0/>)

1. Introduction

High temperature plasmas are generated within magnetic confinement fusion devices - the fusion plasma within the International Thermonuclear Experimental Reactor (ITER) will reach temperatures of 150,000,000°C, and the plasma-facing first wall will be exposed to temperatures of 350°C - 550°C during normal operation [1]. However, turbulent plasma phenomena such as edge localised modes (ELMs), blobs, or disruptions may result in plasma-wall interactions which temporarily raise the temperature of first wall materials beyond their design limits [2–4]. These events may occur thousands of times during the design life of a prototype fusion power station, and repeated strikes to the same surface may result in the accumulation of localised thermal damage and the degra-

ation of underlying materials. The cumulative effects of plasma-wall interactions on the phase regimes, microstructure and material properties of novel fusion reactor materials must be thoroughly understood prior to their use. Plasma-facing components will also experience high fluxes of 14.1MeV neutrons [5] that can damage materials through primary knock-on atom displacement cascades and transmutation [6]. Thus, the degradation mechanisms of first wall materials are likely to be complex.

Ferritic-martensitic 9Cr-1Mo steels are favoured candidate materials for structural applications in fusion reactors due to their excellent radiation swelling resistance and small 50°C increase in ductile to brittle transition temperature (DBTT) under high neutron fluxes [7, 8]. Variants of this steel have been developed by the fusion community that replace elements such as Mo, Nb, and Ni with W, V, and Ta. This strategic substitution eliminates elements that are readily transmuted into long-lived radionuclides under neutron irradiation, as they would otherwise pose a challenge for decom-

* Corresponding author.

E-mail address: dk14424@bristol.ac.uk (D. Kumar).

Table 1
Thermal loads on the EU DEMO first wall arising from plasma phenomena [14–19].

Mode/Excursion	Peak Load MW m ⁻²	Frequency Hz	Duration ms	Impact Factor MJ (m ² s ^{0.5}) ⁻¹
Blobs	0.16 – 0.49	-	5 – 20	-
Unmitigated ELMs	0.6	1 – 0.8	0.6	4-8
Mitigated ELMs	0.1 – 0.2	26	1.2	-
Unmitigated Disruption	100 – 250	-	4	95-128
Mitigated Disruption	75	-	5-10	0.75

missioning and radioactive waste disposal [9]. The resultant materials are known as reduced-activation ferritic-martensitic (RAFM) steels.

Eurofer-97 is the leading RAFM steel candidate for the European and UK fusion programmes. It is the structural material of choice for several ITER tritium breeding blanket test modules including the water-cooled lithium-lead (WCLL) and helium-cooled pebble-bed (HCPB) test breeder blankets [2]. Eurofer-97 is also extensively employed as a structural material in blanket designs for the EU Demonstration Power Station (EU DEMO), a future commercial-scale prototype fusion power station [3, 10–13]. Many breeder blanket designs for EU DEMO feature a first wall comprised of a Eurofer-97 structure armoured with a thin (2 mm) layer of tungsten to protect Eurofer-97 from plasma-wall interactions. The first wall in these designs is often actively cooled by pressurised water or gaseous helium passing through coolant channels within the Eurofer-97 structure [14].

In addition to tungsten armouring, the damaging transient thermal loads in EU DEMO may be mitigated by employing a number of plasma control measures, such as resonant magnetic perturbation (RMP) coils to control edge localised modes (ELMs), and massive gas injection (MGI) and/or shattered pellet injection (SPI) to mitigate disruptions. Estimated transient thermal loads from the literature are given in Table 1.

Thermal energy from these high magnitude, short duration thermal loads may propagate through the plasma-facing tungsten armour to the underlying Eurofer-97 structure, briefly heating it above the maximum temperature limit of 550°C [15]. Repeated exposure to these thermal loads over time may result in the significant evolution of Eurofer-97 microstructure, and lead to the eventual degradation of mechanical and corrosion-resistant properties. This paper explores the effects of short-term high temperature exposure on the microstructure of Eurofer-97 and the effects of both continuous and transient heating.

Prior work on the thermal aging of Eurofer-97 has been previously undertaken by others, but with little consideration of transient thermal loads and at considerably lower temperatures than those explored here [20, 21]. Additionally, high temperature studies on conventional 9-12Cr ferritic-martensitic steels are not directly comparable due to the novel composition and unique phase behaviour of Eurofer-97. Fernandez et al. aged Eurofer-97 at 400°C, 500°C and 600°C for 1000, 5000 and 10,000 hours and observed Cr enrichment at grain boundaries [20]. This was attributed to the presence of M₂₃C₆ chromium precipitates located along grain and sub-grain boundaries, but they did not discount the possibility of Cr diffusion to grain boundaries [20]. The mechanical properties of Eurofer-97 were found to be stable at temperatures up to 600°C, with a 23°C increase in the DBTT perhaps linked to the observation of occasional equiaxed grains replacing martensitic laths. This was attributed to Cr precipitate coarsening on the pinning and mobility of lath interfaces as reported in 9Cr-1Mo steels [22]. Areas of recrystallisation occurred in a F82H steel but overall a similar lack of significant microstructural change was seen in 7-11CrW reduced activation martensitic steels exposed to 250-550°C for up to 13,500 hours [23].

The temperatures explored in this study may occur under off-normal conditions and for relatively short durations, but small suc-

cessive changes to the microstructure of Eurofer-97 may accumulate over time and gradually degrade essential material properties. Structural integrity is an important safety concern for water-cooled tritium breeding blanket concepts, due to the explosion risk posed by hydrogen-producing lithium-water interactions, and the radiological hazard to workers posed by retained tritium in plasma facing materials [15]. Understanding how Eurofer-97 behaves under simulated reactor conditions will be vital to developing a robust safety case for EU DEMO, and will have important implications for the reliability, availability and the economic viability of future fusion power stations.

2. Computational modelling

2.1. Thermal transients arising from plasma-wall interactions

A simulation of mitigated disruption heating on the first wall of the 2019 single module segment (SMS) WCLL breeder blanket for EU DEMO (Fig. 1.a) was undertaken to determine target parameters for the thermal exposure experiments in Section 3. The COMSOL Multiphysics 2019 software was used to perform thermal finite element analysis on a defeatured 2D representation of the WCLL first wall. A time-dependent study with step increments of 0.1 ms was employed with thermal properties from the literature [24]. Thermal stresses were not calculated.

The model of the WCLL first wall was discretised into a mesh of 2,200 2D triangular planar linear heat transfer elements. Element edge length varied from 7.00 to 0.01 mm with smaller elements employed at the tungsten-Eurofer-97 interface to improve local precision. Boundary conditions and interaction properties were configured based on the following assumptions:

- Toroidal symmetry (plane heat transfer).
- Thermal resistance across the tungsten-Eurofer-97 interface is negligible.
- The thermal mass of the PbLi tritium breeding material is such that it is unaffected by disruption heating and remains at a constant initial temperature of 400°C [24].
- Water velocity in the first wall cooling channels is 2.0 m s⁻¹. This yields a convective film coefficient at the cooling water-Eurofer-97 interface of 21,350 W m⁻² K⁻¹ using the Dittus and Boelter approach [25].
- The water in the first wall cooling channels at 155 bar does not exceed its saturation temperature of 345°C and remains single-phase.

To verify material properties, geometry and boundary conditions, normal operation steady state thermal loads were applied to the model from recent literature on WCLL development [26, 27]. The simulation was checked for convergence using the maximum temperature of Eurofer-97 and validated against literature values. The model was found to converge on a solution for maximum Eurofer-97 temperature that agreed with the literature to within ±5°C [24]. To simulate mitigated disruption heating the steady state was perturbed by a heat flux of 75 MW m⁻² applied to the plasma-facing tungsten surface for a duration of 10 ms [15]. The resulting change in temperature of the Eurofer-97 components was studied.

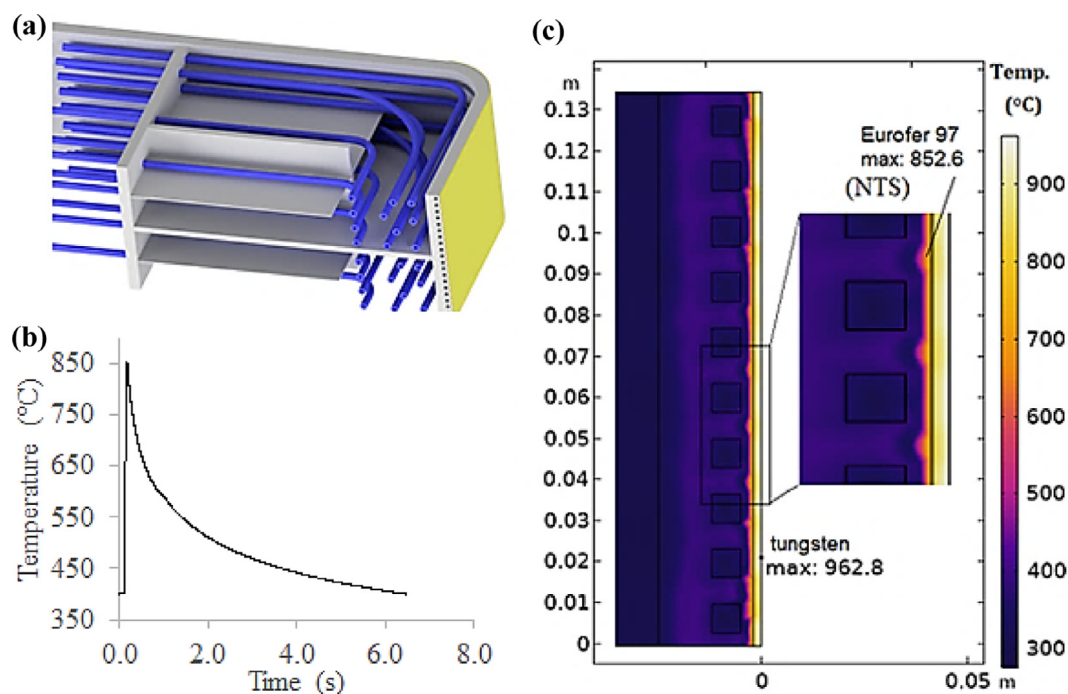


Fig. 1. (a) Cut-away 3D model of the WCLL breeding blanket with plasma-facing tungsten surface in yellow, derived from personal communication (F. Moro, 2019) (b) Plot of maximum WCLL first wall Eurofer-97 temperature versus time during (and after) a mitigated disruption occurring at 0.1s. c) Temperature distribution in the WCLL first wall 0.1 ms after a mitigated disruption.

The simulation revealed that despite the tungsten armour, the temperature of Eurofer-97 regions of the WCLL first wall increases from the normal average operating temperature of 400°C to a maximum of 853°C during a mitigated disruption (Fig. 1.c). This temperature rise occurs in under a second due to the high thermal conductivity of the thin 2 mm plasma-facing tungsten layer ($150 \text{ W K}^{-1} \text{ m}^{-1}$) [28]. However, it is short lived (Fig. 1.b) and thermal energy is quickly removed from the affected area by the first wall water cooling channels and the PbLi tritium breeder material.

The maximum Eurofer-97 temperature is observed at the tungsten-Eurofer interface, where residual stresses from the tungsten joining process may be present and tritium adsorption from the plasma may occur. It is also proximate to the square water-cooling channels of the first wall, where the corrosion-resistance of Eurofer-97 will be of principal concern.

2.2. Eurofer-97 phase evolution

To gain insights into the phase evolution of Eurofer-97, MatCalc thermodynamic modelling software was used to calculate the equilibrium phase fraction diagram of Eurofer-97 with composition 8.89Cr - 1.11W - 0.44Mn - 0.19V - 0.14Ta - 0.12C (wt.%) from Table 2. MatCalc is based on the CALPHAD (Computer Coupling of Phase Diagrams and Thermochemistry) method for thermodynamic calculations.

The literature composition of Eurofer-97 was used to obtain the equilibrium phase fraction diagram from MatCalc in Fig. 2. A significant point can be seen at $\sim 800^\circ\text{C}$ where the phase fraction of ferrite drops to zero and new austenite forms. At this point the fraction of M_{23}C_6 precipitates decreases to zero as the precipitates are taken into solution, but TaC precipitates are still present. Equilibrium austenite transformation temperatures (A1 and A3) were calculated to be 815 and 857°C respectively. These values were not experimentally verified but were compared with dilatometry results (extrapolated to equilibrium) of others and found to exhibit a slight mismatch [29, 30]. For A1 and A3, Danon & Alamo [29] re-

Table 2

A typical composition of Eurofer-97 from literature [13].

Element	Weight %
Cr	8.82 - 8.96
W	1.07 - 1.15
Ta	0.13 - 0.15
V	0.18 - 0.20
Mn	0.38 - 0.49
C	0.11 - 0.12
Fe	Bal

ports circa. 820 and 880°C respectively, while Oliveira [30] reports 829 and 888°C respectively. Oliveira [31] also performed thermochemistry simulations for Eurofer-97 and observed a similar mismatch between experimental values and those predicted by CALPHAD. The formation of new metastable martensite in prior austenite grains is expected to occur as specimens are cooled from austenite temperatures to below the martensite onset temperature, M_s . Estimating the M_s temperature in MatCalc requires data on the driving force for the Eurofer-97's martensitic transformation, which at present appears to be absent from the literature. However, using values typical for the Fe-C system of $1.5\text{--}1.7 \text{ kJ mol}^{-1}$ [32] our simulation yields a M_s temperature of 371–402°C. This agrees well with the Zillyk (2015) experimentally determined value for M_s of 390°C [33].

3. Experimental procedure

3.1. Heat treatment

A plate of Eurofer-97 cast 2 with a composition 9.08Cr-1.07W-0.23V-0.12Ta-0.56Mn-0.10C (in wt.%) [31] was provided by United Kingdom Atomic Energy Authority (UKAEA), Oxfordshire, UK. This material was normalised at 980°C for approx. 0.5h followed by air-

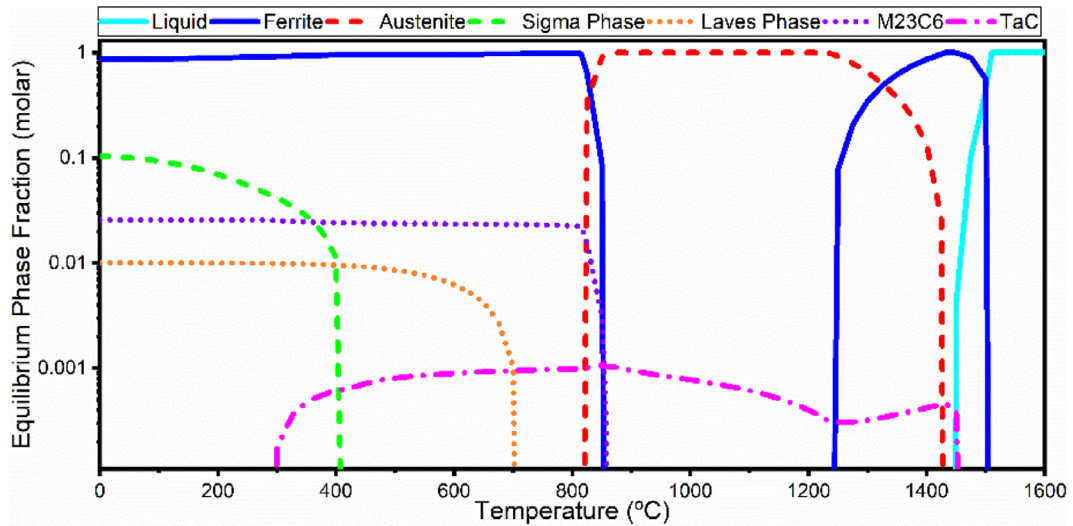


Fig. 2. MatCalc equilibrium phase fraction diagram for Eurofer-97 of composition given in Table 1.

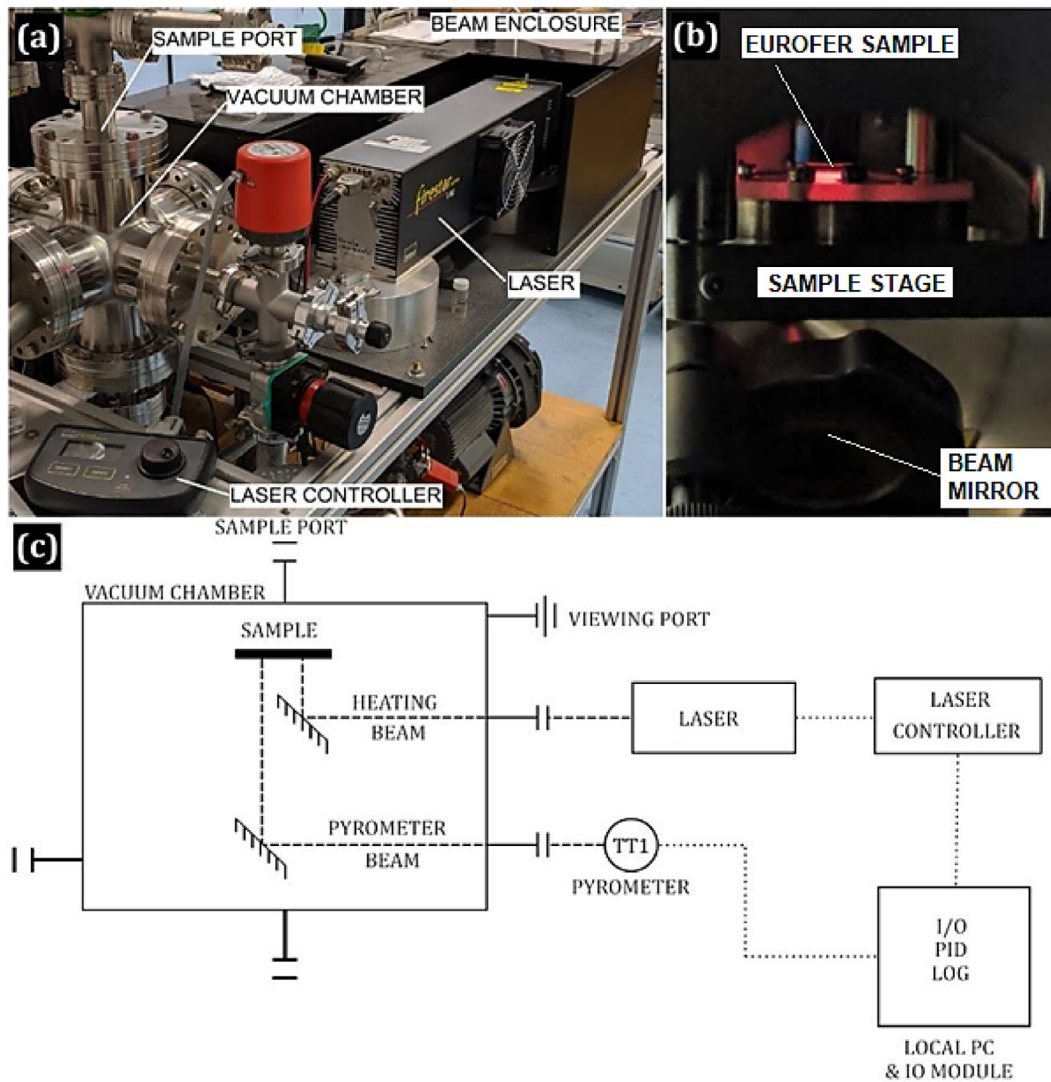


Fig. 3. a) An annotated photograph of the laser apparatus used for transient thermal exposure. b) A sample of Eurofer-97 on the sample stage, glowing red during laser exposure. c) Diagram of the laser heating apparatus.

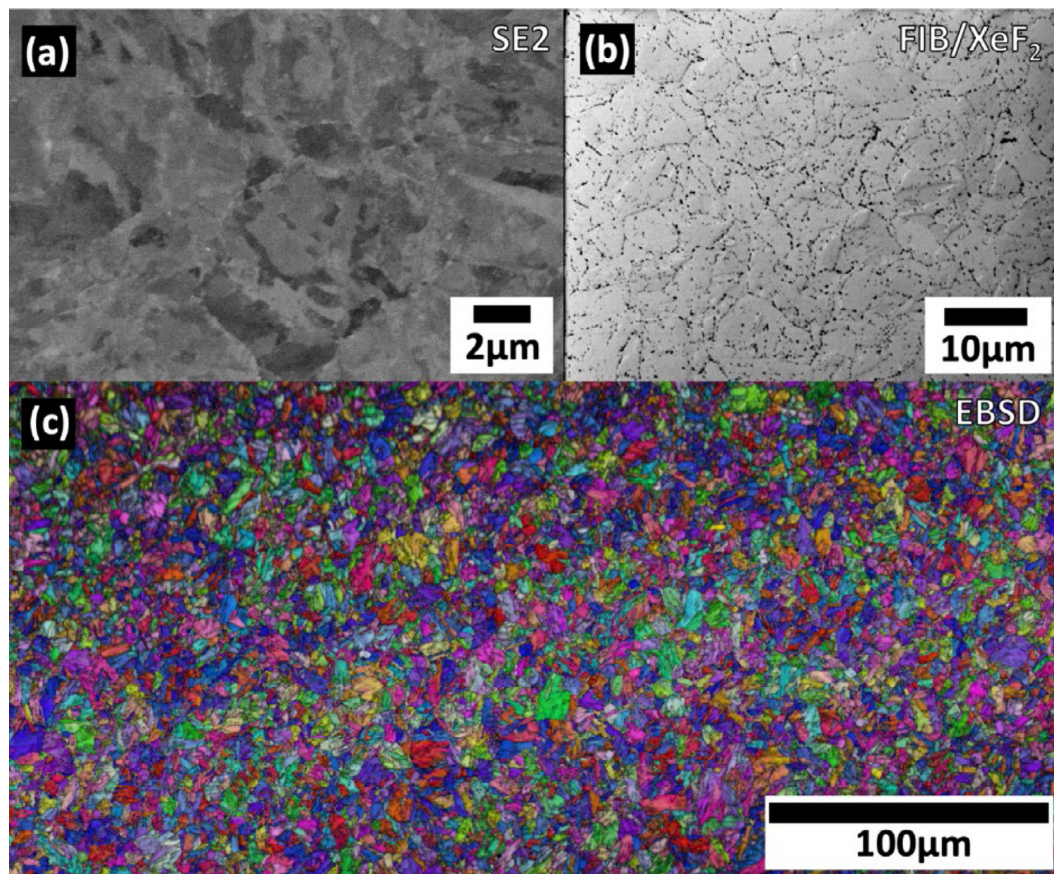


Fig. 4. As-received Eurofer-97 imaged with: (a) SEM secondary electron image; (b) XeF_2 enhanced FIB with carbides in black; (c) EBSD grain orientation map.

quenching, then tempered at 760°C for 1.5h followed by air cooling. This is the ‘reference’ thermomechanical treatment adopted for the qualification of Eurofer-97 for use with ITER and DEMO in the EUROfusion Material Database and Handbook [34]. Two sets of samples were prepared from this material using a Struers Accutom 50 diamond disc cut-off saw. Throughout sectioning, the workpiece was water cooled and the saw feed rate limited to 0.05 mm min⁻¹ to minimise cutting damage. The first set of samples were cut to 6 × 4 × 2 mm³ for use with a continuous heating experiment. These samples were sealed under vacuum in quartz vials and degassed at 680°C. They were subjected to isochronal heat treatment at temperatures of 550°C, 650°C, 700°C, 750°C, 800°C, 850°C, and 950°C for 168 hours. 850°C and 950°C samples were then revisited to explore shorter 4 hour and 24 hour exposures. After ageing the sealed vials were removed and quenched in water.

The second set of Eurofer-97 samples were cut to 8 × 8 × 0.5 mm³ for use with a transient heating experiment. This employed a laser heating apparatus (Fig. 3) that directly applies beam to the sample, enabling rapid and controllable heating. The laser used (Synrad Inc, Firestar V40 series) was a continuous wave CO₂ laser ($\lambda = 10.6 \mu\text{m}$) with linear polarisation and an output power of 40 W. System optical losses are estimated to be 25% thus the maximum power applied to the laser-incident sample face was approximately 30 W. More details about this system can be found elsewhere [35].

Preliminary testing found the laser absorption of the as-prepared Eurofer-97 sample insufficient to rapidly reach the representative maximum temperature predicted by the thermal simulation (Section 2). To improve the laser-material interaction a plasmonic grating coupler was fabricated on each laser-incident face. This comprised of a laser-engraved linear grating on the Eurofer-97

with a period of 10.5 μm and a filling factor of 50%, coated with 50 nm of tungsten via DC magnetron sputtering [36]. The tungsten coating being necessary as steel alloys don’t have plasmonic properties, contrary to tungsten. Reverse (non-laser incident) faces were polished to reduce their emissivity and lower radiative heating losses, and the sample holder was made of quartz to minimise conductive heat losses.

Samples of Eurofer-97 with the plasmonic grating coupler were rapidly heated by the laser apparatus from a base temperature of 400°C to 850°C by operating the laser at full power for 12 s, then passively cooled to 400°C via radiation to the vacuum chamber internals and conduction to the quartz sample holder. This was repeated 1,480 times over a total of 41 hours.

Sample oxidation during high-temperature exposure was minimised by conducting the experiment under vacuum with a chamber base pressure of 7.5×10^{-5} mTorr. The temperature of the laser-incident sample face was continuously monitored throughout the experiment by a non-contact dual-detector ($\lambda = 1.0, 1.5 \mu\text{m}$) infrared spot pyrometer, operated in single colour mode. This instrument has a resolution of 0.1°C and a maximum uncertainty of 2°C. The emissivity of tungsten used ($\varepsilon = 0.35$) was based on literature values [37].

3.2. Specimen preparation for microstructural characterisation

Heat treated specimens were prepared for microstructural analysis by mounting in conductive thermosetting resin and sequential polishing using progressively finer SiC papers to a 5 μm finish, and then subsequently to a 1/4 μm diamond polish in accordance with [38]. A 12 hour 50 nm colloidal silica vibrational polish was used to obtain the final mirror finish. Between each grinding and polish-

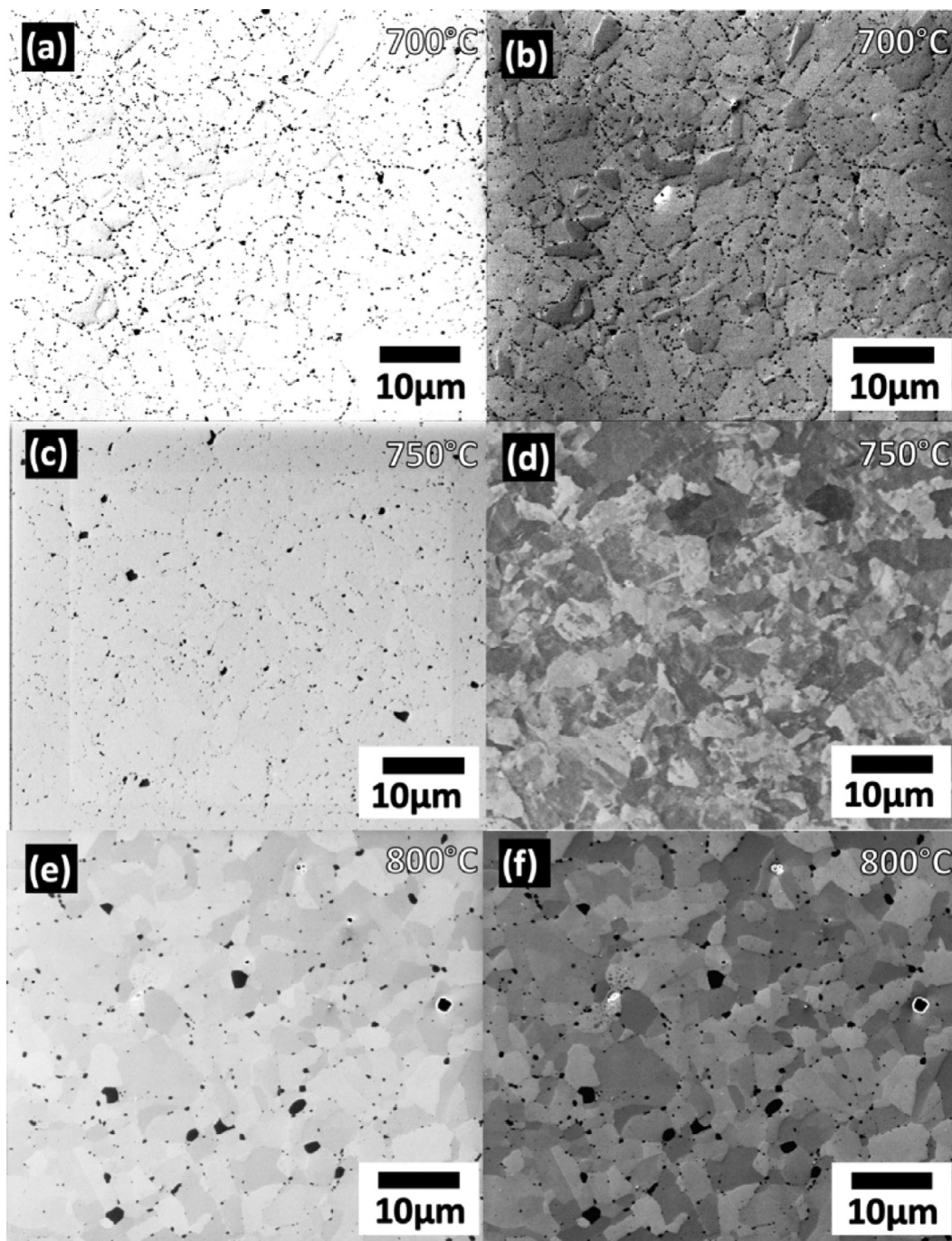


Fig. 5. XeF₂ enhanced FIB images of Eurofer-97 thermally aged for 168 hours at (a,b) 700°C, (c,d) 750°C, and (e,f) 800°C. Left column highlights precipitates in black from XeF₂ enhanced FIB imaging. Right column highlights grain structure as XeF₂ layer is etched away.

ing stage, samples were thoroughly cleaned with detergent to avoid cross-contamination between grits/pastes. At the end of polishing, samples were ultrasonically cleaned and degreased using acetone, ethanol, isopropanol, and distilled water.

3.3. Characterisation techniques

A Zeiss SigmaHD Variable Pressure Field Emission Gun Scanning Electron Microscope (FEGSEM) equipped with secondary electron (SE), angle selective backscatter (AsB), energy dispersive X-ray (EDX), and electron backscatter detector (EBSD) was used for the characterisation of microstructure. Beam acceleration voltages of

10–20kV were employed for imaging. EBSD data was collected with the specimen tilted at 70° to the electron beam, using a voltage of 30kV and a 120µm aperture. EBSD data were collected using a DigiView 3 high-speed camera, run using orientation image mapping (OIM) software (Ametek, Utah, USA).

Focused Ion Beam (FIB) milling was performed using a FEI FIB 201. A 12 nA/30 kV ion beam was used to remove surface oxide from the specimens, which is determined as the point where ion-channelling grain contrast becomes visible. A 150 pA/30 kV beam was used to image the grain structure, prior to the introduction of XeF₂ gas into the chamber. With the beam blanked, gas flow was initiated and allowed to reach a partial pressure of 1.5×10^{-5}

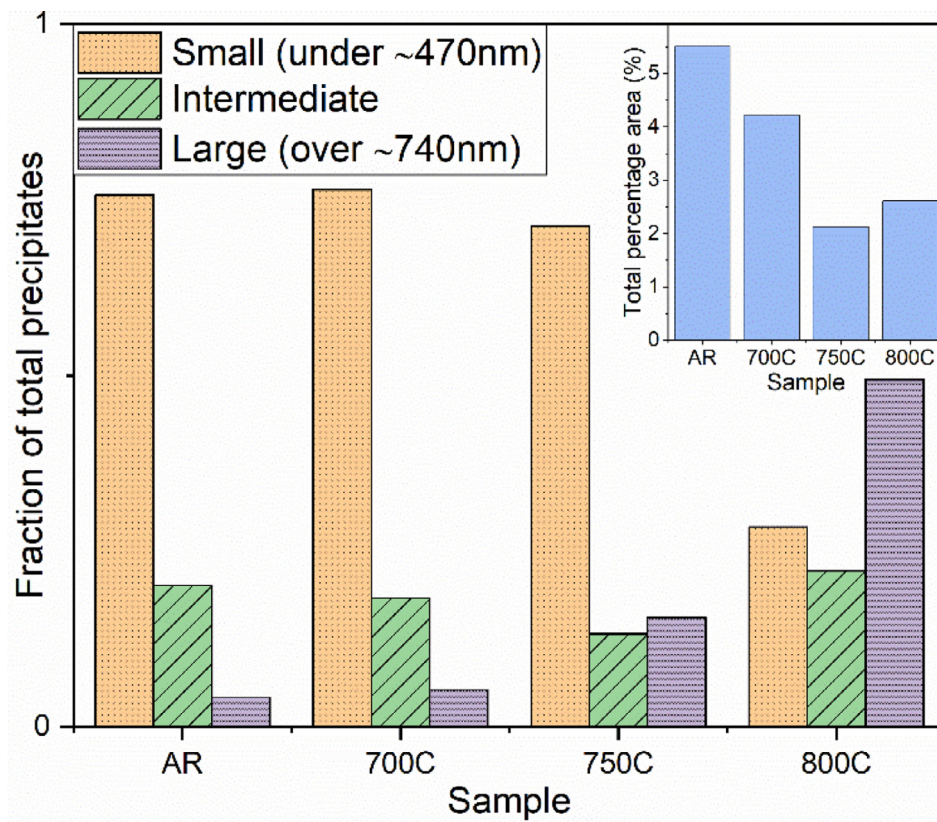


Fig. 6. Counting statistics taken from Fig. 4.b and Fig. 5.a, c, e XeF₂ enhanced FIB images highlighting secondary phase precipitates. Precipitates distinguished by small (< ~470 nm), intermediate, and large (> ~740 nm). Figure shows fraction of total particles in each category and the total percentage area taken up by secondary phase precipitates.

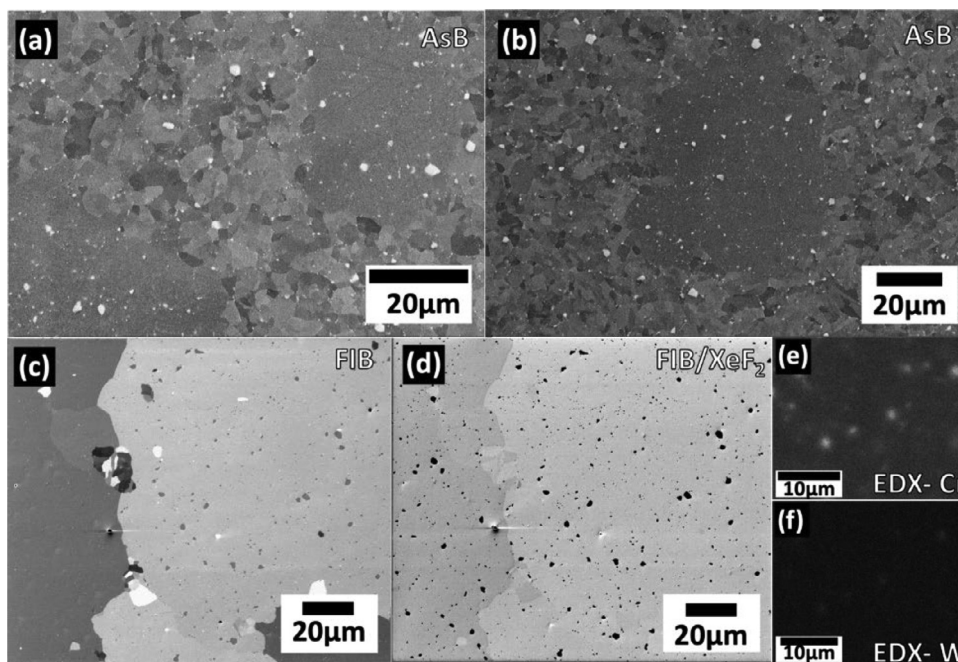


Fig. 7. Eurofer-97 samples aged for 168 hours at 800°C. (a) and (b) SEM images with backscatter detector. Cr-rich precipitates in white. (c) FIB image of large grain region. (d) XeF₂ enhanced FIB of the same region, highlighting Cr-rich precipitates. (e,f) EDX maps showing concentration of Cr and W respectively in precipitates.

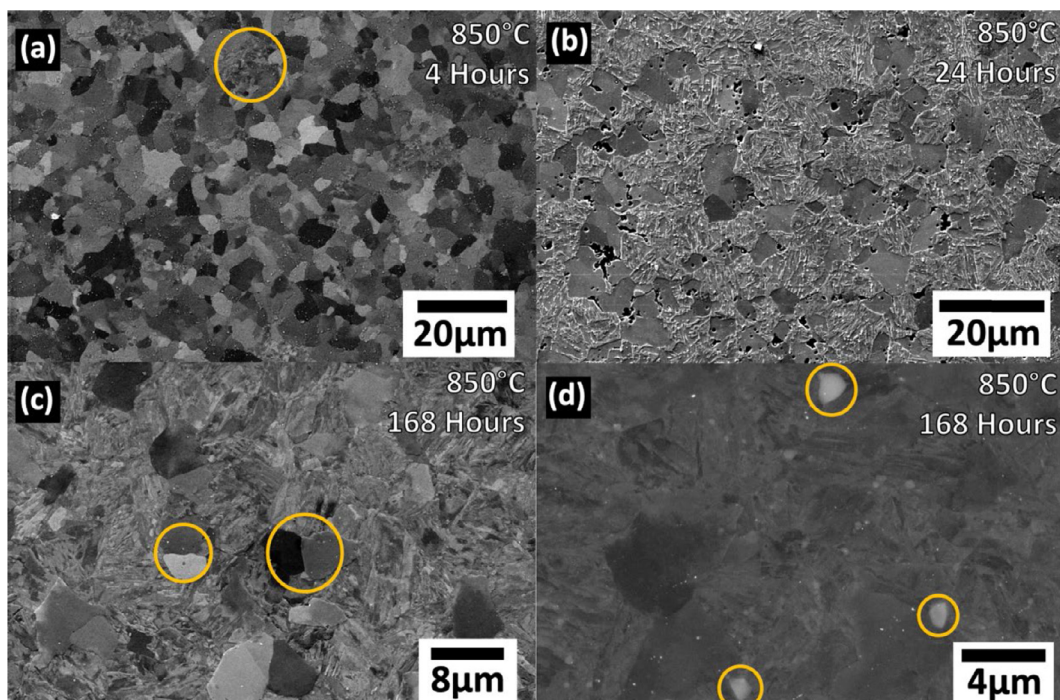


Fig. 8. Eurofer-97 heat treated at 850°C for (a) 4 hours, pocket of martensite circled. (b) 24 hours, increased formation of new martensite. (c) 168 hours, mostly martensite with misaligned ferrite grain pairs circled. (d) Backscatter image after 168 hours. Cr-rich secondary phases circled, largest with diameter ~1700nm.

mbar before the flow was stopped. After a few seconds of rapid beam scanning at 150 pA/30 kV to allow for excess-gas to be sputtered away, imaging was resumed. As per previous work [39] the XeF_2 adhered to the oxide-free metal surface and not the carbide precipitates. Whilst a full description of the process is beyond the scope of this paper, the XeF_2 gas increases the secondary electron yield of the metal surface and improves contrast to highlight the carbides [39]. Counting statistics were obtained using a series of simple image processing tools, including a custom LabView script for area % counting. This used thresholds of 50 pixels and 125 pixels to define between coarse, intermediate/agglomerate, and fine precipitates. These correspond to feature diameters of ~470 nm and ~740 nm respectively, assuming a spherical precipitate. Particle sizes were chosen arbitrarily in order to distinguish between single large precipitates and agglomerations of smaller precipitates forming the 'intermediate' group.

4. Results

4.1. Microstructure of as-received Eurofer-97

Fig. 4 shows that as-received (AR) Eurofer-97 has a tempered martensitic microstructure with laths of length 0.1 - 2 μm occurring in prior austenite grains with diameters of 5 - 12 μm . The XeF_2 enhanced FIB imaging (Fig. 4.b) reveals the homogeneous distribution of ~400 nm diameter carbide precipitates preferentially at prior austenite grain boundaries [39]. An EBSD scan (Fig 4.c) shows the as-received microstructure to be isotropic with a high degree of homogeneity.

4.2. Furnace-aged Eurofer-97

No significant microstructural change was observed for Eurofer-97 thermally aged at 550°C and 650°C for 168 hrs compared with the as-received condition. However, using XeF_2 enhanced FIB imaging in Fig. 5 reveals that there is secondary phase coarsening at

higher temperatures up to 800°C. Fig. 5 shows samples aged for 168 hours at 700 - 800°C with XeF_2 enhanced FIB imaging. The right hand column highlights the grain structure of aged samples as XeF_2 is etched away whilst the left hand column highlights secondary phase precipitates due to XeF_2 adherence to the bulk [39]. EDX of secondary phase precipitates shows they are Cr-rich with compositions ranging from 20 wt.% at 750°C up to 30 wt.% for the largest precipitates at 800°C compared to ~8.89 wt.% in the overall composition from Table 2.

Fig. 6 shows the counting statistics obtained from the analysis of the precipitate sizes in the XeF_2 enhanced FIB data in Figs. 4.b and 5. Precipitates are grouped into small (< ~470 nm diameter), intermediate, and large (> ~740 nm diameter). Fig. 6 shows the fraction of total precipitates present in each sample fall into which size category. The total percentage area of the surface covered by secondary phase precipitates is also shown in the top right corner.

It is also observed in Fig. 7 that Eurofer-97 aged for 168 hours at 800°C results regions with significantly larger grains (~100 μm) than those of the as-received Eurofer-97 (< 10 μm Fig. 4). Fig. 7.d shows the same FIB imaged area as that in Fig. 7.c but with XeF_2 introduced to highlight the coarsened precipitates. Fig. 7.e, f show the concentration of Cr and W in these precipitates via EDX. Point spectra taken from precipitates in Fig. 7.e, f gave a Cr concentration of (19 ± 2) wt.% and (3.1 ± 0.5) wt.% for W compared to 8.89 wt.% and 1.11 wt.% expected from Table 2.

Fig. 8.c shows that after 168 hours at 850°C the microstructure changes significantly to a new martensitic lath structure with few misaligned ferrite grains remaining. Fig. 8.a, b show the progression of this change at shorter durations (4 hours, 24 hours). We also note the presence of a Cr secondary phase after 168 hours similar in size to those after 168 hours at 800°C (Fig. 8.d).

After 168 hours at the highest investigated temperature, 950°C, the sample is ~100% martensite within prior-austenite grains (Fig. 9). This microstructure also developed after shorter times (24hours) in Fig. 9.a, b. The Cr-rich precipitates were taken into so-

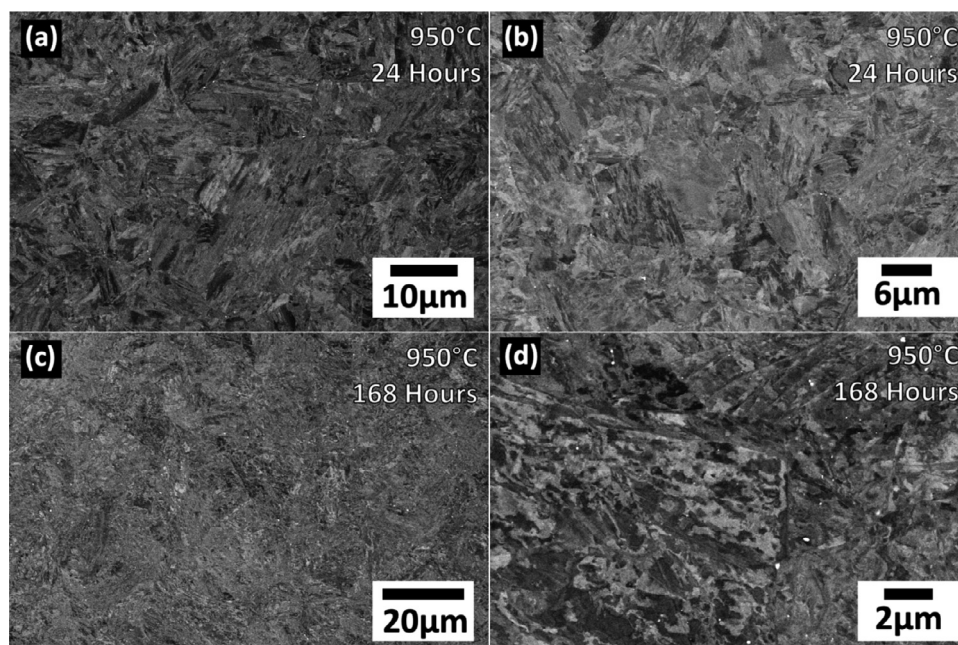


Fig. 9. Eurofer-97 SEM secondary electron images of sample heat treated at 950°C for (a,b) 24 hours and (c,d) 168 hours showing new martensitic lath structure in prior austenite grains.

lution with only small ~100 nm diameter Ta-rich MX precipitates found via EDX with 6 – 12 wt.% vs bulk (0.15 ± 0.34) wt.%.

4.3. Laser-exposed Eurofer-97

The CO₂ laser was used to heat a representative $8 \times 8 \times 0.5$ mm sample of Eurofer-97 from 400°C to ~850°C in ~12 seconds. This was repeated a total of 1,480 times over 41 hours, with the sample allowed to cool down to 400°C via radiation to sample chamber walls before each repeat. The mean peak sample temperature was 846°C (SD = 14.7°C). The repetition rate was limited by cooling time which resulted in a mean transient event duration (including cooling time) of 104 seconds. Fig. 10 shows a subset of the temperature readings obtained during 10 simulated mitigated disruptions.

Characterisation (Fig. 11) of Eurofer-97 exposed to 1,480 transient heating events revealed a significant grain size increase compared with the as-received Eurofer-97. Grain size was measured by the ImageJ software and the average was found to have increased from 0.1 – 2 µm to 5 – 40 µm. Additionally, the characteristic martensite laths observed in Fig. 4 were notably absent, and the microstructure was found to have transformed to predominantly ferrite plus carbide precipitates (Fig. 11) with EBSD (Fig. 11.d) showing that only a few small packets of martensite remain. New coarsened precipitates were found to be abundantly distributed throughout the laser exposed Eurofer-97 and were located at both grain boundaries (intergranular) and inside ferrite grains (intragranular). The precipitates were found to be Cr-rich (Fig. 11.f) with typical composition shown in Table 3.

Fig. 12 shows EBSD grain orientation maps for samples aged in the furnace for 168 hours in comparison to the laser-exposed sample. At 650°C and 700°C the tempered martensitic lath structure was similar to that of the as-received sample (Fig. 4.c), although with approximately 2x larger mean grain diameter. At 800°C larger (~16 µm) grains are present amongst a sea of smaller (mean of ~5 µm) equiaxed grains as we observe less of the as-received lath structure. At 850°C there is a clear transformation to new martensitic laths in prior austenite grains, but some ferrite remains. The area fraction of ferrite vs. martensite in this sample was estimated

Table 3

Composition of a typical Cr-rich precipitate post laser exposure (from EDX).

Element	Weight %
C	1.54
N	2.82
O	1.2
V	0.65
Cr	17.07
Fe	74.4
Ta	0.4
W	1.92

to be ~11% vs. 89% by analysing the image quality maps from EBSD. This method was put forward in [40] as the BCT structure of martensite is very close to the ferrite BCC and therefore hard to distinguish via EBSD apart from small differences in image quality between the phases. There is then a fully martensitic structure observable at 950°C. The laser-exposed sample differs from the furnace samples where it is seen to have significantly larger (mean of ~19 µm) equiaxed ferrite grains.

Fig. 13 shows how grain diameter has changed with the heat treatments. Grain diameters of the samples furnace aged for 168 hours at 800°C and 850°C are not dissimilar to the as-received grain size with most below 10 µm, despite the original martensitic lath structure being replaced with equiaxed ferrite grains at 800°C and the presence of new martensite at 850°C in Fig. 12. The sample aged at 950°C for 168 hours and the laser exposed sample exhibit the largest increase in grain diameter from the as-received specimen. For the 950°C aged sample this contribution is from new martensitic laths forming in large (mean of ~17 µm) prior-austenite grains. The laths are longer than other samples but narrow compared to the large equiaxed ferrite grains seen in the laser exposed Eurofer-97. The average grain size in the laser exposed sample is ~19 µm compared to ~4 µm for the as-received sample, nearly a 5x increase.

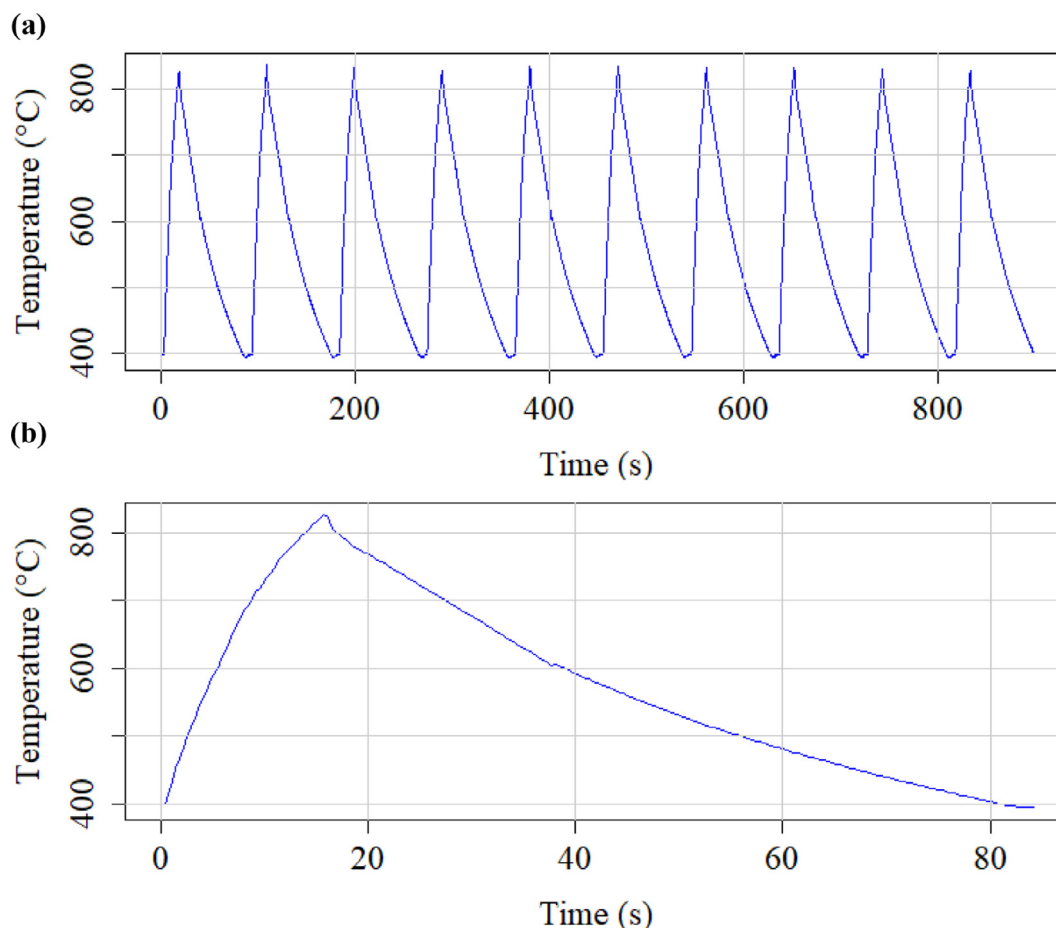


Fig. 10. Pyrometer measurements of Eurofer-97 sample temperature during a) 10 of the 1,480 transient heating events, b) a single heating event.

5. Discussion

Since there are no measurements available for thermal transients arising in a fusion reactor of the size of ITER or DEMO, the modelling of thermal transient behaviour in a WCLL fusion breeder blanket component has been simulated using COMSOL Multiphysics. The model predicted that during a mitigated disruption, thermal transients up to 853°C can occur with a total excursion time above operating temperature of approximately 6 s (Fig. 1.b). The equilibrium phase diagram for Eurofer-97 modelled using MatCalc shows a transition from ferrite to austenite and dissolution of $M_{23}C_6$ in the 800–850°C region, and so whilst an individual thermal transient approaches this temperature regime for a very short time period, it is uncertain what the cumulative effect of such disruptions may give to the material microstructure. This provided the rationale for a study on the effect of cumulative short thermal excursions on the microstructure of Eurofer-97.

As a baseline, the isochronal ageing of Eurofer-97 was demonstrated using furnace exposure at temperatures between 550 and 950°C for a week, as well as several shorter tests for certain temperature conditions of interest. Major observed microstructural changes include (i) the coarsening of secondary phase precipitates up to 800°C, (ii) the decomposition of the tempered martensite structure above 800°C, and (iii) significantly increased average grain sizes.

Microanalysis using SEM-EDX of secondary phase precipitates in both furnace-aged (Fig. 7.e, f) and laser exposed samples (Fig. 11.f) revealed them to be Cr-rich. The equilibrium phase diagram (Fig. 2) suggests that these precipitates are likely $M_{23}C_6$ with some TaC

carbides also expected. These precipitates grow larger as the heat treatment temperature increases (Fig. 5), leading to a sparse distribution of larger carbides (up to ~2 μm diameter) after 168 hours at 800°C. The area fraction of these precipitates in furnace aged samples (Fig. 6) decreased from the 5.5% in the as-received sample to that 2.1% after ageing at 750°C for 168 hours, and to 2.6% after 168 hours at 800°C, where the majority of precipitates are now ‘large’ (> ~740 nm). Below 800°C the number of ‘large’ precipitates increases with the temperature of heat treatments, but the main contribution to the total percentage area was from ‘small’ (< ~470 nm) precipitates. Overall, analysis confirms the observation of coarsening of Cr rich precipitates and a decrease in the proportion of smaller carbides. As precipitates coarsen with temperature the overall area covered by secondary phases decreases. Conversely, precipitates in F82H steel under irradiation have been found to decrease in size potentially resulting in two competing processes for Eurofer-97 within the fusion reactor [41, 42]. After 168 hours at 950°C, coarse Cr rich precipitates are no longer present and only small (~100 nm) Ta-rich precipitates remain. Only TaC precipitates are expected to stable at equilibrium conditions at this temperature and so it is likely that Cr-rich $M_{23}C_6$ precipitates have dissolved at 950°C.

For samples aged for 168 hours at different temperatures, microstructural changes were observed in line with MatCalc thermodynamic modelling. Fig. 2 shows that there should be no new phases observed below ~800°C and that ferrite is the bulk equilibrium phase. This is confirmed by Fig. 12 where the tempered ferritic-martensitic structure remains after 168 hours 650°C and 750°C and we see equiaxial ferrite grains at 800°C as the as-

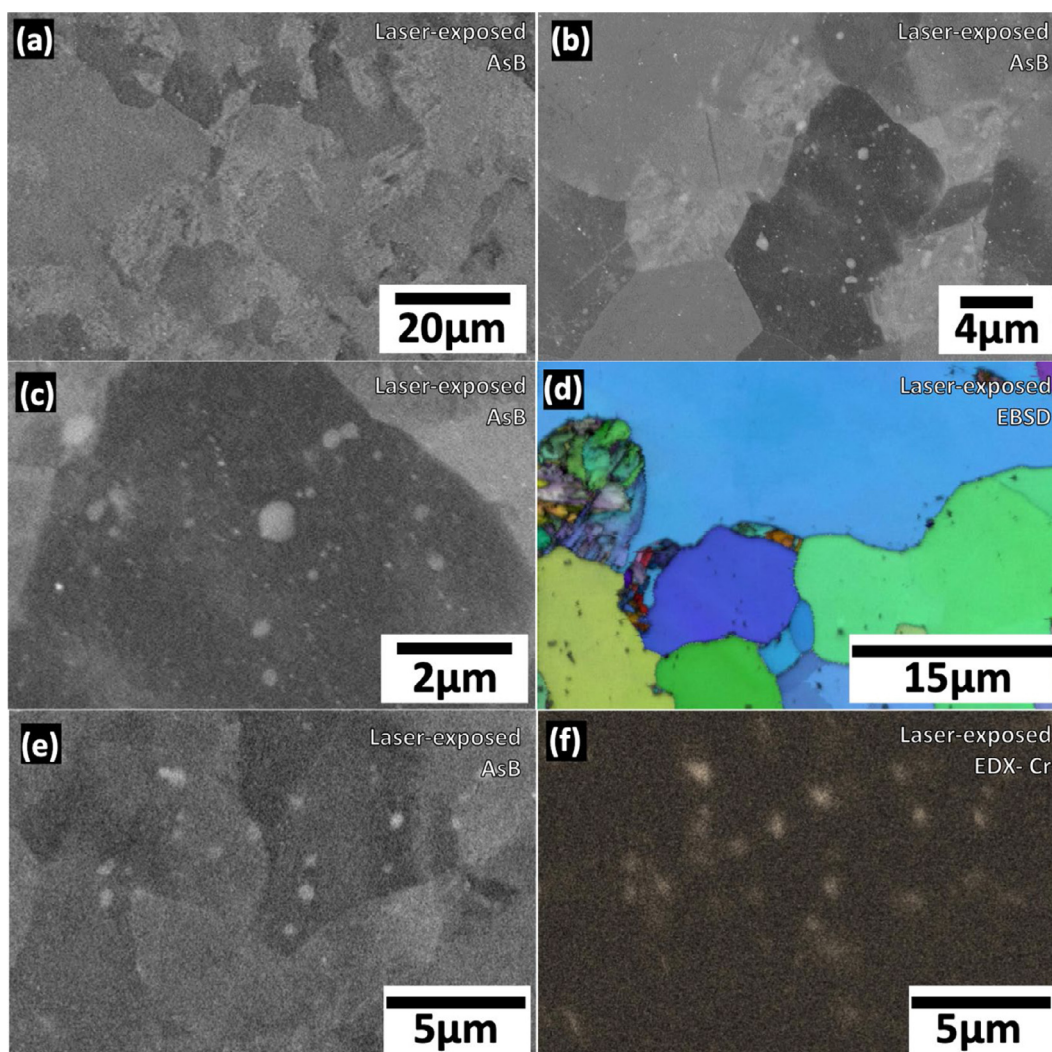


Fig. 11. Micrographs of laser-exposed Eurofer-97 imaged via: (a) 1kX AsB, (b) 10kX AsB, (c) 10kX AsB, (d) EBSD. (e) and (f) show the same area with AsB and EDX showing Cr concentration respectively.

received microstructure begins to decompose. Above this temperature austenite should begin to form as the new equilibrium phase (Fig. 2) which, upon quenching, instantaneously transforms into a metastable martensitic lath structure. This new martensite forms in samples aged for 168 hours at 850°C and 950°C (Figs. 8, 9, 12). Fig. 13 indicates how these phase changes affect the grain size. After 168 hours at 650°C and 750°C the grain sizes increase to approximately twice the as-received size. Conversely, after 168 hours at 800°C and 850°C the average grain size remains similar to that of the as-received sample (Fig. 13), likely due to nucleation of new austenite dominating rather than growth of existing grains. After 168 hours at 950°C the microstructure transitions fully to newly formed martensite in prior austenite grains that are, on average, over three times larger in diameter than in the as-received tempered ferritic-martensitic grains.

Changes were also observed after shorter durations of furnace exposure. Packets of new martensite were seen after just 4 hours at 850°C with the transition to new martensite in prior austenite grains seen progressing after 24 hours (Fig. 8.a, b). Thermodynamic modelling suggests austenite and TaC should be the equilibrium phases at this temperature (Fig. 2) which implies these short durations are not enough to achieve total equilibrium. This is seen as misoriented ferrite grains and suspected coarse $M_{23}C_6$ precipitates still remain after 168 hours (Fig. 8.c, d) where they should

no longer be present (Fig. 2). At 950°C the microstructure is fully martensite after only 24 hours (Fig. 9.a, b). This shows that even short exposures to the higher temperatures can result in significant microstructural change.

To understand better how repeated short thermal cycling can affect the microstructure, Eurofer-97 were cycled between 400°C (expected operating temperature of Eurofer-97 components) and 850°C for 1480 pulses approximately 12s in length using a custom designed laser rig inside a vacuum chamber. Greater changes in grain structure are seen in the laser exposed specimen in Fig. 11, including large intragranular Cr-rich carbides and grains with a more ferritic character clean of martensitic laths. In the laser exposed samples grains are seen to span a much larger range of sizes from 5 – 40 µm (Fig. 13). In practice, the laser-exposed sample spends the majority of the time at temperatures below 800/850°C (Fig. 10) which is the temperature regime where grain growth is observed for the furnace aged samples (Fig. 13). Therefore, more time spent in this lower temperature regime could explain why we observe 5 – 40 µm equiaxial ferrite grains and carbide precipitates coarsening, leading to decomposition of desired ferritic-martensitic microstructure, and no new phases forming.

In the laser experiment, the sample of Eurofer-97 was allowed to naturally cool to its normal in-service operating temperature of 400°C between laser transients, instead of being quenched to room

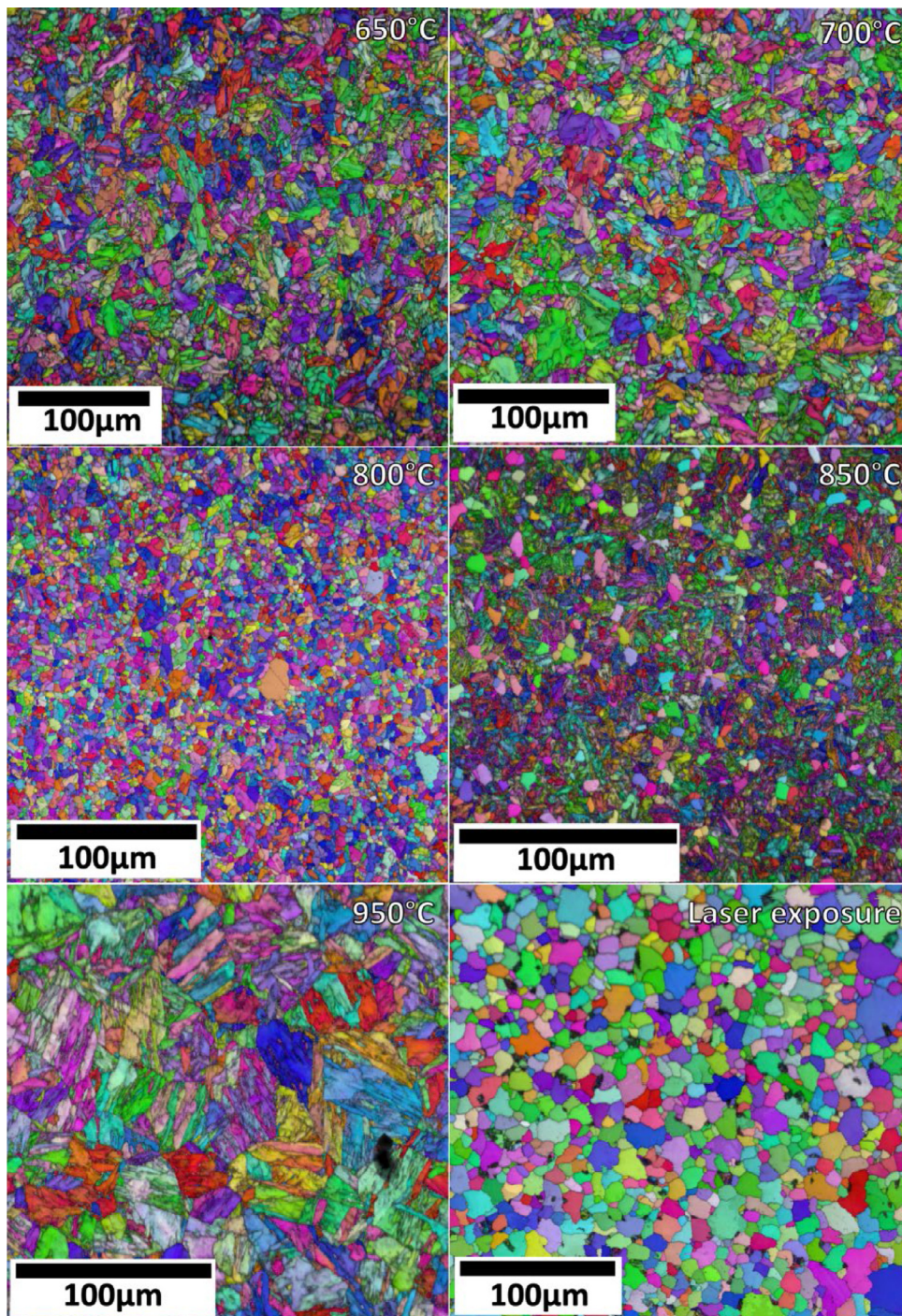


Fig. 12. EBSD grain orientation maps for samples isochronally aged for 168 hours as well as for the laser-transient treatment.

temperature as with the furnace-aged specimens. Cooling here is slower than expected within a reactor cooling loop. FEA results (Fig. 1.b) suggest that, due to the water cooling employed by the WCLL breeder blanket design, Eurofer-97 may be subjected to cooling rates of $\sim 65^\circ\text{C s}^{-1}$ after each mitigated disruption thermal transient. At present, the laser apparatus does not allow the cooling rate of the sample to be controlled, however the estimated cooling rate of 7.5°C s^{-1} is well above the critical cooling rate reported by Danon (2002) [29] of $0.06^\circ\text{C s}^{-1}$ (210°C h^{-1}) for an austenisation temperature of 980°C . However samples are cooled to just above the M_s temperature, 390°C [33], between each laser pulse which limits martensite formation resulting in the observed, pre-

dominantly ferrite microstructure (Figs. 11–12). Danon also report an increase in both A1 and A3 by $\sim 40^\circ\text{C}$ with an increase in heating rate from 0.1 to 10°C s^{-1} [29]. With the laser sample heated at $\sim 40^\circ\text{C s}^{-1}$ this implies that a greater increase in austenisation temperatures may be present in the laser exposed sample leading to less transformation to martensite. The significantly altered microstructure after laser pulsing is an important finding as it is more closely analogous to in-reactor conditions.

Understanding the role of plasma-wall interactions in the long-term degradation of first wall structural materials is an essential step in developing a robust safety case for EU DEMO. Coarsening of Cr-rich secondary phases, formation of new martensite in prior

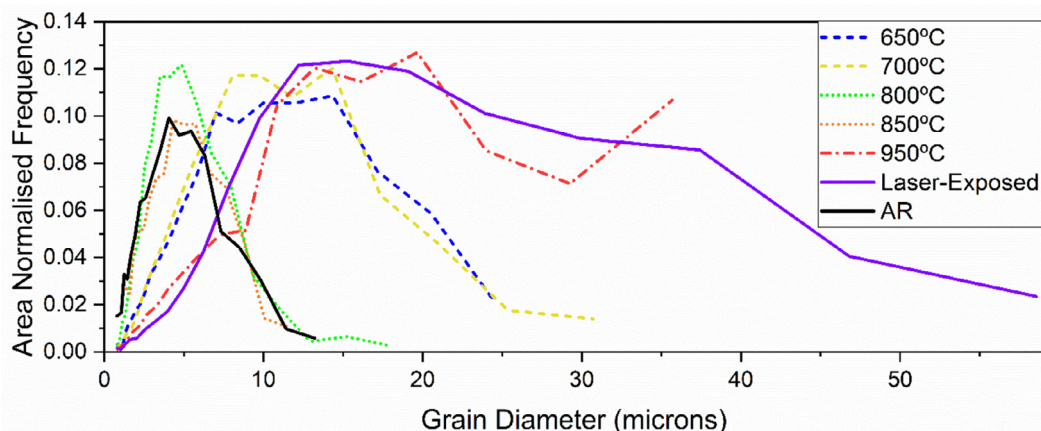


Fig. 13. Area normalised frequency vs. grain diameter obtained from EBSD data for furnace samples aged for 168 hours and the laser-exposed sample (as in Fig. 12) compared to the as-received sample (Fig. 4.c).

austenite grains, and increases in grain size are all changes that could affect mechanical properties of Eurofer-97. Larger grain sizes and carbide precipitate coarsening would affect dislocation movement and coarsening of Cr-rich precipitates could also cause sensitisation to corrosion behaviour pertinent to WCLL breeder blanket design. Secondary phase carbide precipitates may also contribute to the pinning of martensitic laths, therefore coarsening may accelerate the decomposition of the as-received tempered martensitic microstructure [22, 23]. High temperature creep behaviour may also be affected, as grain boundary carbides have been found to promote the nucleation and growth of intergranular creep cavities [43].

Whilst the laser exposure rig allows the microstructural changes of cycled thermal transients to be explored, the pulse length of 12s is still longer than might be expected from a fusion plasma excursion. There is scope to modify the laser apparatus with a cooling system to enable cooling rates to more closely match those estimated by the simulation work. Future work could explore transient heating effects on other fusion materials including oxide dispersion strengthened (ODS) Eurofer-97, a variant that employs a homogenous dispersion of nano oxides to improve high temperature creep behaviour, as the implications of results presented here on ODS Eurofer-97 are not yet known. Presently, nearly all leading candidates for breeder blankets of EU DEMO employ conventional Eurofer-97 steel [3, 10–13]. There are also ramifications of this work for the effects of plasma-wall interactions on oxide-dispersed variants of Eurofer-97, and the tungsten-Eurofer-97 joint, where the maximum Eurofer-97 temperatures are expected.

6. Conclusions

Computational simulations using COMSOL Multiphysics show that breeder-blanket structural materials in nuclear fusion reactors may be exposed to higher than normal operating temperatures up to 850°C due to plasma-first wall contact events, at which temperatures the calculated equilibrium phase diagram predicts that microstructural changes will occur. Eurofer-97 components of the DEMO first wall are predicted by the model to briefly reach such temperatures during mitigated plasma disruptions, which may occur thousands of times during a DEMO plasma campaign. Specimens of Eurofer-97 were thermally aged in a furnace for 168 hours up to 950°C as well as heated via a pulsed CO₂ laser in order to simulate the effect of thermal transients.

The microstructure of Eurofer-97 was significantly altered after exposures to temperatures between 650°C and 950°C and subse-

quent quenching. After 168 hours at 650°C and 750°C the average grain diameter approximately doubled. For 168 hour exposures at 700°C to 800°C, coarsening of Cr-rich secondary phase precipitates was observed. Above 850°C martensitic packets within newly formed prior austenite grains nucleated throughout the material after 168 hours. Partial transformation to these new martensite packets was observed even after short (4 hour) exposures to 850°C, with fully martensitic microstructure in new prior austenite grains after 24 hours at 950°C.

While a fusion reactor will not see these high temperatures in the continuous condition, it may be subjected to repeated transient exposures for short times that reach these conditions. To test this influence on the microstructure, Eurofer-97 was also laser-exposed in a custom designed vacuum system to mimic thermal transients to the temperatures predicted by the finite element modelling. Samples heated repeatedly from 400°C - 850°C for transients lasting 12 seconds showed coarsening of Cr-rich intergranular and intragranular precipitates as well as large, 5 - 40 μm, equiaxed ferrite grains.

Significant microstructural changes have been observed in this study that indicate that thermal transients may influence the microstructure of fusion components with longer plasma durations and reactor operational lifetimes. Whilst further study is required to fully characterise this behaviour, such microstructural changes could affect the material properties in terms of ductility, creep behaviour, and corrosion resistance and therefore are important in the consideration of fusion plant design and operation.

Declaration of Competing Interest

The authors declare that they have no known competing financial interests or personal relationships that could have appeared to influence the work reported in this paper.

CRediT authorship contribution statement

D. Kumar: Conceptualization, Methodology, Software, Formal analysis, Investigation, Writing – original draft, Writing – review & editing, Visualization. **J. Hargreaves:** Conceptualization, Methodology, Software, Formal analysis, Investigation, Writing – original draft, Writing – review & editing, Visualization. **A. Bharj:** Methodology, Investigation. **A. Scorrer:** Methodology, Investigation. **L.M. Harding:** Investigation, Formal analysis, Resources. **H. Dominguez-Andrade:** Methodology, Investigation, Resources, Writing – review & editing. **R. Holmes:** Writing – review & editing. **R. Burrows:**

Writing – review & editing, Resources. **H. Dawson:** Writing – review & editing, Resources. **A.D. Warren:** Methodology, Investigation, Writing – original draft, Writing – review & editing, Formal analysis. **P.E.J. Flewitt:** Writing – original draft, Writing – review & editing. **T.L. Martin:** Conceptualization, Methodology, Writing – original draft, Writing – review & editing, Supervision, Funding acquisition.

Acknowledgments

The authors would like to thank UKAEA/CCFE for the provision of a representative specimen of Eurofer-97. D. Kumar would like to thank EPSRC and NNL for the funding of his doctoral training partnership PhD project (S108151-136), and J. Hargreaves would like to thank the Centre for Doctoral Training in Nuclear Energy Futures for funding his PhD (UK EPSRC grant EP/S023844/1). Dr Neil Fox, Dr James Smith and Mr Gary Wan are thanked for their assistance with the laser apparatus. Dr Fabio Moro is thanked for providing design data and drawings of the WCLL.

References

- [1] M. Abdou, et al., Blanket/first wall challenges and required R&D on the pathway to DEMO, *Fusion Eng. Des.* (2015).
- [2] L. Giancarli, et al., Test blanket modules in ITER: an overview on proposed designs and required DEMO-relevant materials, *J. Nucl. Mater.* 367–370 (Aug. 2007) 1271–1280.
- [3] F. Romanelli, et al., Fusion electricity: a roadmap to the realisation of fusion energy, *EFDA* (2012).
- [4] H. Bolt, et al., Materials for the plasma-facing components of fusion reactors, *J. Nucl. Mater.* 329–333 (Aug. 2004) 66–73.
- [5] R. Aymar, P. Barabaschi, Y. Shimomura, The ITER design, *Plasma Phys. Control. Fusion* 44 (2002) 519–565.
- [6] R. Lässer, et al., Structural materials for DEMO: the EU development, strategy, testing and modelling, *Fusion Eng. Des.* 82 (5–14) (2007) 511–520.
- [7] Z. Tong, Y. Dai, The microstructure and tensile properties of ferritic/martensitic steels T91, Eurofer-97 and F82H irradiated up to 20 dpa in STIP-III, *J. Nucl. Mater.* 398 (1–3) (2010) 43–48.
- [8] K. Shiba, A. Hishinuma, Low-temperature irradiation effects on tensile and Charpy properties of low-activation ferritic steels, *J. Nucl. Mater.* 283–287 (2000) 474–477 no. PART I.
- [9] D.R. Harries, G.J. Butterworth, A. Hishinuma, F.W. Wiffen, Evaluation of reduced-activation options for fusion materials development, *J. Nucl. Mater.* 191–194 (Sep. 1992) 92–99.
- [10] <https://www.iter.org/sci/iterandbeyond>, “After ITER,” 2019. [Online]. Available: <https://www.iter.org/sci/iterandbeyond>. [Accessed: 18-Jan-2019].
- [11] Y. Poitevin, et al., Progresses and challenges in supporting activities toward a license to operate European TBM systems in ITER, *Fusion Eng. Des.* 89 (7–8) (Oct. 2014) 1113–1118.
- [12] J. Aubert, G. Aiello, N. Jonquères, A.Li L. Puma, A. Morin, G. Rampal, Development of the water cooled lithium lead blanket for DEMO, *Fusion Eng. Des.* 89 (7–8) (Oct. 2014) 1386–1391.
- [13] R. Lindau, et al., Present development status of EUROFER and ODS-EUROFER for application in blanket concepts, *Fusion Eng. Des.* (2005).
- [14] A. Del Nevo, et al., WCLL breeding blanket design and integration for DEMO 2015: status and perspectives, *Fusion Eng. Des.* 124 (Nov. 2017) 682–686.
- [15] R. Wenninger, R. Albanese, R. Ambrosino, F. Arbeiter, J. Aubert, The DEMO wall load challenge, *Nucl. Fusion* 57 (4) (2017) 1–11.
- [16] T.N. Todd, Pulsed DEMO Design Assessment Studies, *Fusion Sci. Technol.* 64 (2) (2013) 76–85.
- [17] P. Domalpalay, M. Dellabianca, Thermal-hydraulic design of water cooled first wall of the fusion reactor under DEMO conditions, *Fusion Eng. Des.* 124 (Dec. 2017) 311–315.
- [18] Y. Igitkhanov, R. Fetzer, B. Bazylev, Effect of heat loads on the plasma facing components of demo, *Fusion Eng. Des.* 109–111 (Dec. 2016) 768–772.
- [19] R.P. Wenninger, et al., DEMO divertor limitations during and in between ELMs, *Nucl. Fusion* 54 (11) (Dec. 2014) 114003.
- [20] P. Fernández, M. García-Mazarió, A. Lancha, J. Lapeña, Grain boundary microchemistry and metallurgical characterization of Eurofer97 after simulated service conditions, *J. Nucl. Mater.* 329–333 (Aug. 2004) 273–277.
- [21] P. Fernández, A. Lancha, J. Lapeña, M. Serrano, M. Hernández-Mayoral, Metallurgical properties of reduced activation martensitic steel Eurofer97 in the as-received condition and after thermal ageing, *J. Nucl. Mater.* 307–311 (Dec. 2002) 495–499.
- [22] W.B. Jones, C.R. Hills, D.H. Polonis, Microstructural evolution of modified 9Cr-1Mo steel, *Metall. Trans. A* 22 (5) (1991) 1049–1058.
- [23] Y. De Carlan, A. Alamo, M.H. Mathon, G. Geoffroy, A. Castaing, Effect of thermal aging on the microstructure and mechanical properties of 7-11 CrW steels, *J. Nucl. Mater.* 283–287 (2000) 672–676.
- [24] P.A. Di Maio, P. Arena, G. Bongiovì, P. Chiovaro, A. Del Nevo, R. Forte, Numerical assessment of the thermomechanical behaviour of the DEMO Water-Cooled Lithium Lead inboard blanket equatorial module, *Fusion Eng. Des.* 136 (Dec. 2018) 1178–1185.
- [25] F.W. Dittus, L.M.K. Boelter, Heat transfer in automobile radiators of the tubular type, *Int. Commun. Heat Mass Transf.* 12 (1) (1985) 3–22.
- [26] P. Arena, A. Del Nevo, P.A. Di Maio, R. Forte, G. Nevone, Parametric thermal analysis for the optimization of Double Walled Tubes layout in the Water Cooled Lithium Lead inboard blanket of DEMO fusion reactor, *J. Phys. Conf. Ser.* 1224 (Dec. 2019) 12031.
- [27] F. Edemetti, E. Martelli, A. Tassone, G. Caruso, A. Del Nevo, DEMO WCLL breeding zone cooling system design: Analysis and discussion, *Fusion Eng. Des.* 146 (Sep. 2019) 2632–2638.
- [28] V. Philipps, Tungsten as material for plasma-facing components in fusion devices, *J. Nucl. Mater.* 415 (1) (May 2011) S2–S9 Supplement.
- [29] A. Danón, A. Alamo, Behavior of Eurofer97 reduced activation martensitic steel upon heating and continuous cooling, *J. Nucl. Mater.* 307–311 (1 SUPPL) (2002) 479–483.
- [30] V.B. Oliveira, H.R.Z. Sandim, D. Raabe, Abnormal grain growth in Eurofer-97 steel in the ferrite phase field, *J. Nucl. Mater.* 485 (Mar. 2017) 23–38.
- [31] V.B. Oliveira, K.D. Zilnyk, H.R.Z. Sandim, Thermodynamic Simulation of Reduced Activation Ferritic–Martensitic Eurofer-97 Steel, *J. Phase Equilibria Diffus.* 38 (3) (2017) 208–216.
- [32] M. Palumbo, Thermodynamics of martensitic transformations in the framework of the CALPHAD approach, *Calphad Comput. Coupling Phase Diagrams Thermochem.* 32 (4) (2008) 693–708.
- [33] K.D. Zilnyk, V.B. Oliveira, H.R.Z. Sandim, A. Möslang, D. Raabe, Martensitic transformation in Eurofer-97 and ODS-Eurofer steels: a comparative study, *J. Nucl. Mater.* 462 (2015) 360–367.
- [34] E. Gaganidze, F. Gillemot, I. Szenthe, M. Gorley, M. Rieth, E. Diegele, Development of EUROFER97 database and material property handbook, *Fusion Eng. Des.* 135 (February) (2018) 9–14.
- [35] H. Dominguez-Andrade, A. Croot, G. Wan, J.A. Smith, N.A. Fox, Characterisation of thermionic emission current with a laser-heated system, *Rev. Sci. Instrum.* 90 (4) (2019).
- [36] S. Nunez-Sanchez, H.D. Andrade, J. Harwood, I. Bickerton, N.A. Fox, M.J. Cryan, Molybdenum gratings as a high-temperature refractory platform for plasmonic heat generators in the infrared, *Micro. Nano Lett.* 13 (9) (2018) 1325–1328.
- [37] L.I. International, SPOT Pyrometer User Guide 808273, Dronfield, U.K., 2018.
- [38] A.D. Warren, A.I. Martinez-Ubeda, O.D. Payton, L. Picco, T.B. Scott, Preparation of Stainless Steel Surfaces for Scanning Probe Microscopy, *Micros. Today* 24 (03) (2016) 52–55.
- [39] C. Liu, P.J. Heard, O.D. Payton, L. Picco, P.E.J. Flewitt, A comparison of two high spatial resolution imaging techniques for determining carbide precipitate type and size in ferritic 9Cr-1Mo steel, *Ultramicroscopy* 205 (2019) 13–19 no. December 2018.
- [40] M.M. Nowell, S.I. Wright, J.O. Carpenter, Differentiating ferrite and martensite in steel microstructures using electron backscatter diffraction, *Mater. Sci. Technol. Conf. Exhib.* 2009, MS T09 2 (2009) 933–943 no. January 2009.
- [41] S. Kano, et al., Instability of MX and M23C6 type precipitates in F82H steels under 2.8 MeV Fe²⁺ irradiation at 673 K., *Nucl. Mater. Energy* 17 (2018) 56–61 no. November 2017.
- [42] S. Kano, et al., Study of radiation-induced amorphization of M23C6 in RAFM steels under iron irradiations, *J. Nucl. Mater.* 533 (2020) 152088.
- [43] J. Chen, K. Yoon, S.-T. Tu, Creep Behavior of Pressurized Tank Composed of Functionally Graded Materials, *J. Press. Vessel Technol.* 133 (5) (Jul. 2011).